Geophysical and Astrophysical Fluid Dynamics
Vol. 00, No. 00, 00 Month 2023, 1–16

The nonlinear evolution of two surface quasi-geostrophic vortices

Xavier Carton †*, Jean N. Reinaud ‡, Armand Vic † and Jonathan Gula (IUF member) †
† LOPS/IUEM/UBO, Brest, France
‡ School of Mathematics and Statistics, University of St Andrews, UK.
(*Received 00 Month 20xx; final version received 00 Month 20xx*)

We investigate numerically the evolution of a baroclinic vortex in a two-level surface quasi-geostrophic model. The vortex is composed of two circular patches of uniform buoyancy, one located at each level. We vary the vortex radii, the magnitude of buoyancy, and the vertical distance between the two levels. We also study different radial profiles of buoyancy for each vortex. This paper considers two main situations: firstly, initially columnar vortices with like-signed buoyancies. These vortices are contra-rotating, are linearly unstable and may break. Secondly, we consider initially tilted vortices with opposite-signed buoyancies, which may align vertically. Numerical experiments show that (1) identical contra-rotating vortices break into hetons when initially perturbed by low azimuthal modes; (2) unstable, vertically asymmetric, contra-rotating vortices can stabilise nonlinearly more often than vertically symmetric ones, and can form quasi-steady baroclinic tripoles; (3) co-rotating vortices can align when the two levels are close to each other vertically, and when the vortices are initially horizontally distant from each other by less than three radii; (4) for initially more distant vortices, two such vortices rotate around the plane center; (5) in all cases, the vortex boundaries are disturbed by Rossby waves. These results compare favorably to earlier results with internal quasi-geostrophic vortices. Further modelling efforts may extend the present study to fully three dimensional ocean dynamics.

Keywords: Two-level model, surface quasi-geostrophy, vortex stability, Burger number, modal analysis

1. Introduction

Vortices are long-lived oceanic features, with a mostly horizontal circulation constrained by the Earth rotation and by the density stratification (Richardson 1983, McWilliams 1991). Vortices play a substantial role in the transfer of water masses, heat and momentum across the oceans (Provenzale 1999, Gula *et al.* 2019, 2022). Insofar as the hydrostatic and geostrophic balances mostly hold for the mesoscale oceanic vortices (i.e. vortices with a radius of a few tens of kilometers and a turn-over period of a few days), the quasi-geostrophic (QG) model is an appropriate framework to describe their dynamics (Reinaud *et al.* 2022). Nevertheless, due to the ocean's density stratification, more than one layer, or vertical level, is necessary to adequately represent these vortices (Reinaud 2019).
An often-used model for vortex dynamics is the two-layer, (internal) quasi-geostrophic model (Flierl 1978). This model represents two superimposed slabs of homogeneous fluid, of different densities, interacting via their density interface. In each layer, the dynamics is governed by the evolution of the potential vorticity (Charney 1948). This two-layer quasi-geostrophic model has been the framework of the study of baroclinic instability of parallel flows (Phillips 1954) and of circular vortices (Sokolovskiy and Verron 2013, Flierl 1988, Carton and McWilliams 1996, Carton *et al.* 2010). Baroclinically unstable vortices can evolve nonlinearly into hetons (Hogg and Stommel 1985a,b, Reinaud and Carton 2009b), contra-rotating ellipses (Carton and McWilliams 1996) or in baroclinic tripoles (Reinaud and Carton 2009a, Sokolovskiy and Carton 2010). Such nonlinear evolutions are also observed in two-layer ageostrophic shallow-water flows (Baey and Carton 2002).

*Corresponding author:xcarton@univ-brest.fr

In the presence of buoyancy anomalies concentrated vertically over a shallow depth, the quasi-geostrophic model can be expressed via the evolution of buoyancy (or temperature) anomalies, which are the singular equivalents of potential vorticity. This restriction of the general QG model is the surface quasi-geostrophic model (SQG); it represents the advection of buoyancy anomalies at the surface and bottom of the ocean, or of a part of the ocean, vertically (Bretherton 1966, Held *et al.* 1995, Lapeyre 2017, Smith and Bernard 2013). The SQG model has been used mostly in a one-level configuration for vortex and turbulence studies (Carton 2009, Carton *et al.* 2011, Tulloch and Smith 2009, Lapeyre and Klein 2006, Klein *et al.* 2008, Harvey and Ambaum 2011, Harvey *et al.* 2011, Badin and Poulin 2019). A SQG model coupled with an internal quasi-geostrophic model has also been used for the study of coupled surface flow-internal vortex Perrot *et al.* (2010), Reinaud *et al.* (2016, 2017a,b). The two-level SQG model was also used to calculate the linear instability of vertically shear, parallel flows by Eady (1949).

Recently, the present authors have investigated the linear stability of a circular vortex in a two-level, SQG model (Vic *et al.* 2022), comprising surface and bottom uniform buoyancy anomalies. Such vortices are here referred to, as Eady vortices by analogy with the Eady problem. The aim of the present work is to extend the linear stability study of two-level Eady vortices to their nonlinear dynamics, that is, investigate the possible formation of hetons (e.g. Gryanik (1983), Hogg and Stommel (1985a,b)), or of more complex compound vortex, from these two-level vortices. For two like-signed buoyancy anomalies, one on each surface, we assess the finite-amplitude evolution of monochromatic angular perturbations, and the possibility of vortex breaking, or of topological rearrangement of the initial vortices. The structure and regularity, or lack thereof, of the final compound vortex cannot be assessed from the linear analysis previously carried out. We also extend our previous study to parameter regimes which are not accessible to linear analysis, for the sake of simplicity and of tractability of the analytical solutions. Finally, we study the ability of initially tilted, two-level SQG vortices, to straighten up. This process, called vertical vortex alignement, has previously been studied in a two-layer internal quasi-geostrophic model (Polvani 1991). It is essential for the robustness and the durability of oceanic vortices.

This paper is organized as follows: we present the SQG model equations, the initial conditions and the numerical implementation in section 2. In section 3, we address the nonlinear evolution of an initially perturbed, contra-rotating Eady vortex, with like-signed temperature anomalies at both levels. These anomalies are initially aligned vertically and they are linearly unstable to perturbations. We assess the influence of various physical parameters on the nonlinear evolution of the vortices. In section 4, we consider the case of two circular, opposite-signed, temperature anomalies, initially horizontally offset. The vortices of such a tilted Eady vortex are co-rotating. We study numerically the possible vertical alignment of the two buoyancy patches at finite time. A discussion on the stability of these Eady vortices follows in section 5. Finally, conclusions are drawn in section 6.

2. Physical and numerical model

2.1. *Model equations and initial conditions; physical parameters*

2.1.1. *Model equations*

In the quasi-geostrophic model, the Coriolis acceleration mostly balances the horizontal pressure gradient and the horizontal velocity is essentially non-divergent. The dynamic

pressure p^* (total pressure minus pressure at rest) is related to a streamfunction ψ^* via $\psi^* = p^*/\rho_0 f_0$. The superscript $*$ indicates a dimensional variable. The Coriolis parameter is $f_0 = 2\Omega\sin(\lambda)$ with Ω the Earth rotation rate and λ the latitude. The density ρ^* is also related to the streamfunction via the buoyancy $b^* = -g\rho^*/\rho_0 = f_0\partial_{z^*}\psi^*$, where ρ_0 is a reference density. Here x^*, y^*, z^* are also dimensional space variables; typically, x^*, y^* vary over tens of kilometers and z^* over hundreds of meters.

The surface quasi-geostrophic (SQG) model assumes that the potential vorticity q^* is zero in the fluid :

$$q^* = \left[\frac{\partial^2}{\partial x^{*2}} + \frac{\partial^2}{\partial y^{*2}} + \partial_{z^*}\left[\left(\frac{f_0^2}{N^2}\right)\partial_{z^*}\right]\right]\psi^* = 0, \quad z^* \in (-h^*, 0),$$

where N is the Brunt-Väisälä frequency, and h^* is the total (dimensional) depth of the fluid layer under study (thus it may be different from the total depth of the ocean). The SQG model assumes that the potential vorticity is concentrated at the surface and at the bottom of the fluid layer under consideration : $q^* = q_1\delta(z^* = 0) + q_2\delta(z^* = -h^*)$ with δ the Dirac distribution. Then, the potential vorticity conservation equation becomes an equation for buoyancy evolution on these two surfaces (Bretherton 1966).

$$\frac{\mathrm{db}^*}{\mathrm{dt}} = \partial_{t^*}b^* + J(\psi^*, b^*) = 0, \quad z^* = 0, -h^*, \tag{1}$$

where $b^* = f_0\partial_{z^*}\psi^*$.
Assuming that the fluid domain is horizontally unbounded, the streamfunction can be written as

$$\psi(x^*, y^*, z^*, t^*) = \int\int A^*_{k^*l^*}(t^*)\ \phi_{k^*l^*}(z^*)\ \exp(\mathrm{i}[\mathrm{k}^*\mathrm{x}^* + \mathrm{l}^*\mathrm{y}^*])\,\mathrm{dk}^*\,\mathrm{dl}^*,$$

where k^*, l^* are the horizontal wavenumbers, b_1^*, b_2^* the Fourier transforms of the surface and bottom buoyancies, and $A^*_{k^*l^*}, \phi_{k^*l^*}$ the Fourier transforms of the associated streamfunctions. Assuming the Brunt-Väisälä frequency constant ($N = N_0$), the condition of zero potential vorticity in the bulk of the fluid leads to

$$\phi''_{k^*l^*}(z^*) - \frac{K^{*2}N_0^2}{f_0^2}\phi_{k^*l^*}(z^*) = 0,$$

where $K^{*2} = k^{*2} + l^{*2}$. This leads to

$$\phi_{k^*l^*}(z^*) = \phi^{(1)}_{k^*l^*}\cosh(K^*N_0z^*/f_0) \ + \ \phi^{(2)}_{k^*l^*}\cosh(K^*N_0(h^* + z^*)/f_0).$$

This simple form of the Fourier transform of ψ provides simple relations between $\phi^{(1)}, \phi^{(2)}$ and the Fourier coefficients of buoyancy at the upper and lower levels, $b^{(1)}(k,l), b^{(2)}(k,l)$, via the relation $b = f_0\partial_z\psi$. This also indicates that the time variability of the Fourier coefficients of ψ and of b are given by the same functions $A^*_{k^*l^*}(t^*)$.

Now we move from dimensional to dimensionless variables. Hereafter, we set $Z^* = N_0z^*/f_0$ and $H^* = N_0h^*/f_0$. Here, H^* is the first internal radius of deformation (in dimensional terms).
We let $1/f_0$ be our time scale, and the vortex radius at the ocean surface, R_1, our length scale. Therefore, the normalized values of f_0 and of R_1 are unity. We define a dimensionless depth in the model $Z = Z^*/R_1$ and a dimensionless radius of deformation $R_d = N_0h^*/(f_0R_1)$. Note that the latter is also a normalised height of the model $H^*/R_1 = H$. The horizontal coordinates are normalised similarly, $x = x^*/R_1, y = y^*/R_1$. The dimensionless time is $t = f_0t^*$. We also normalise the wavenumbers $k = k^*R_1, l = l^*R_1, K^2 = k^2 + l^2$. The streamfunction is

normalised as $\psi = \psi^*/(R_1^2\ f_0)$. The dimensionless buoyancy is $b = \partial_Z \psi = b^*/(f_0 R_1)$.

Then, we have

$$b(x, y, Z = 0, t) = \int\int b_1(k, l, t)\ \exp(\mathrm{i}[\mathrm{kx} + \mathrm{ly}])\,\mathrm{dk}\,\mathrm{dl},$$

$$b(x, y, Z = -H, t) = \int\int b_2(k, l, t)\ \exp(\mathrm{i}[\mathrm{kx} + \mathrm{ly}])\,\mathrm{dk}\,\mathrm{dl},$$

and the normalised streamfunction is

$$\psi(x, y, Z = 0, t) = \int\int \psi_1(k, l, t)\ \exp(\mathrm{i}[\mathrm{kx} + \mathrm{ly}])\,\mathrm{dk}\,\mathrm{dl}, \tag{2}$$

$$\psi(x, y, Z = -H, t) = \int\int \psi_2(k, l, t)\ \exp(\mathrm{i}[\mathrm{kx} + \mathrm{ly}])\,\mathrm{dk}\,\mathrm{dl}, \tag{3}$$

where

$$\psi_1(k, l, t) = \frac{b_1(k, l, t)}{K \tanh(KH)} - \frac{b_2(k, l, t)}{K \sinh(KH)},$$

$$\psi_2(k, l, t) = \frac{b_1(k, l, t)}{K \sinh(KH)} - \frac{b_2(k, l, t)}{K \tanh(KH)}.$$

These forms of ψ at the surface and at the bottom result from the dimensionless equation $b = \partial_z \psi$, using the $\cosh(Kz)$ and $\cosh(K(H + z))$ form of the Fourier coefficients of ψ mentioned above.
Note that these formulae correspond to a vertically bounded domain (between 0 and $-H$), without any flow nor buoyancy anomaly below $-H$.

Material conservation of buoyancy allows us to march b_1, b_2 in time, and these fields can then be inverted to obtain the streamfunction from equations (2) and (3).

2.1.2. *Initial conditions and aim of the simulations*

Our two-level SQG model is initialized with a single disk of uniform buoyancy at each level (surface and bottom). The corresponding streamfunction is given in Vic *et al.* (2022). Figure 1 shows the geometry of the configuration.

We consider the interaction of two vertically aligned vortices with like-signed buoyancy in section 3, and of two horizontally offset vortices with opposite-signed buoyancy in section 4. It should be noted that any axisymmetric distribution of buoyancy corresponds to a steady state. Hence in the present case, the pair of circular, co-axial, vortices is steady. In section 3, we perturb the vortex boundary with a monochromatic perturbation, with angular (or azimuthal) mode m. We assess whether the vortices break, and/or, rearrange as new types of vortices such as dipoles or tripoles. In section 4, we horizontally offset the centres of the two vortices and we study their vertical re-alignment with respect to the horizontal offset and to the vertical distance between the SQG levels.

2.1.3. *Physical parameters*

In this study, the vortex radii R_1, R_2, the deformation radius R_d, the buoyancy magnitudes B_1, B_2, and the angular (or azimuthal) mode m are the physical parameters under consideration. R_1 is fixed as a reference length. It should be noted that increasing B_1 while keeping B_2/B_1 fixed simply modifies the time derivative of buoyancy. Indeed, this rate of change scales as $f_0 B_1$. Therefore, the 4 independent dimensionless physical parameters are

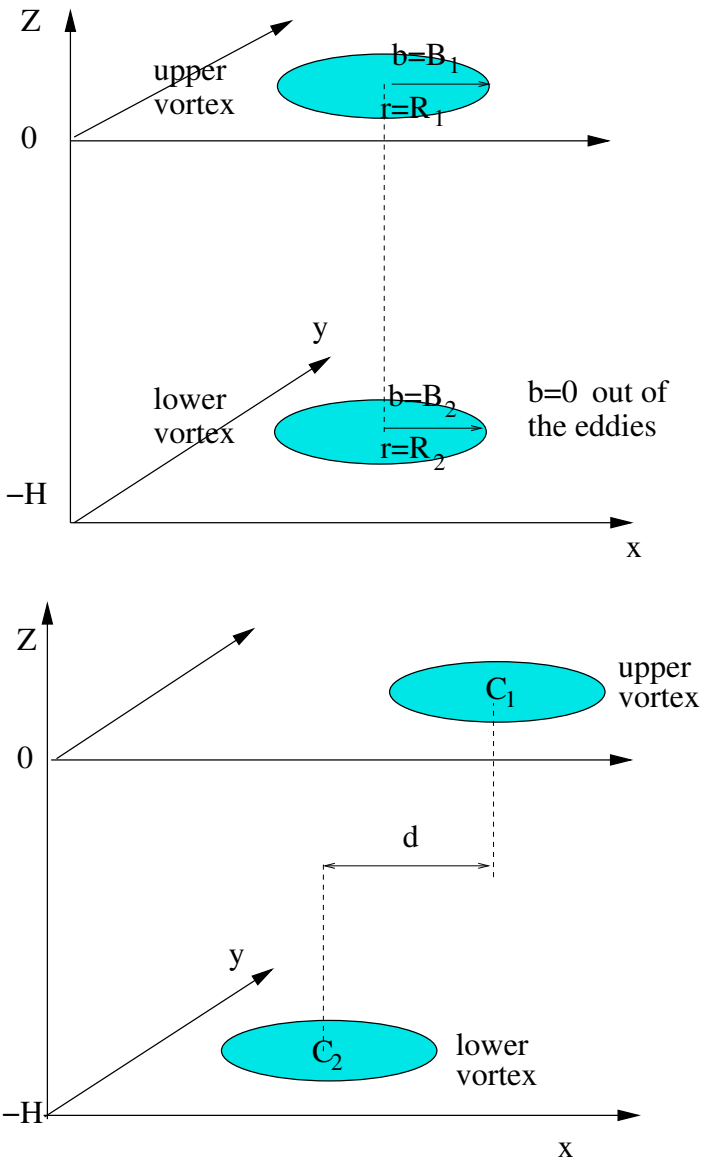

Figure 1. Schematic representation of the two-level SQG model with the two vortices vertically aligned (top) and laterally shifted (bottom).(Colour online).

B_2/B_1, R_2/R_1, $R_d/R_1 = H$ and m.

Due to the large number of parameters, we start by studying a reference case, for which the first two parameters are set to 1. Then we perform a sensitivity study of the instability to the physical parameters by varying them separately.

2.2. *Numerical model*

Our numerical model is a pseudo-spectral model with 256×256 collocation points. We increase the horizontal resolution to 512×512 points for specific analyses. The equations are marched in time with a mixed Euler-Leapfrog scheme with an Euler step every 50 time steps. The Leapfrog scheme is conservative in energy but tends to separate the even and odd solutions.

This is taken care of with the periodic use of an Euler time step. The spatial derivatives are computed in Fourier space and FFT's are used to transform the fields from physical to Fourier space and back. The domain size is $4\pi \times 4\pi$ (except for a few simulations of vortex alignment, when the vortices are initially distant from each other; then the domain size is $8\pi \times 8\pi$). Very weak hyperviscosity is used (biharmonic diffusion) with $\nu_4 = 8 \cdot 10^{-7}$ at 256-resolution and $\nu_4 = 5 \cdot 10^{-9}$ at 512-resolution. The numerical model has been validated in a previous study of vortex merger (Oulhen *et al.* 2022).

3. Nonlinear evolution of linearly unstable SQG vortices with like-signed buoyancy anomalies

Here, we study the various nonlinear regimes of linearly unstable, two-level SQG vortices, for various values of $B_2/B_1 > 0$, R_2/R_1, R_d/R_1 and of the angular mode of perturbation m. We start by considering initially vertically aligned vortices.

3.1. *Vortices with equal radii and intensity*

3.1.1. *An overview of the nonlinear regimes of the vortex depending on its size and on the deformation radius*

Firstly, we set $B_2/B_1 = 1$, $R_2/R_1 = 1$, that is, the two patches constituting the vortex have equal radii and buoyancy magnitudes. We run several simulations, varying $R_d/R_1 = H$. We perturb both buoyancy patches with a mode of deformation $m = 2$.

For $R_d/R_1 = 1$ and 0.6, the Eady vortices elongate elliptically in each layer and eventually break into two hetons (see Figure 2). This is also the case for baroclinically unstable vortices in the two-layer (internal) quasi-geostrophic model (Helfrich and Send 1988). For $R_d/R_1 = 0.5$, the Eady vortices break over a mixed angular mode $m = 2$ and $m = 4$ (with a complex elliptical and square deformation) leading to several fragments. For $R_d/R_1 = 0.4$, angular mode $m = 4$ prevails and the Eady vortices break into four hetons. Finally, for $R_d/R_1 = 0.2$, angular mode $m = 6$ is dominant in the vortex evolution.

Clearly, higher modes of deformation become more unstable as the two levels get closer to each other vertically. This is explained by the connection between the horizontal and vertical scales in the SQG model (this link is due to the vanishing potential vorticity). Short horizontal scales have a short vertical reach. As the two vortices get closer vertically, their small scale perturbations can interact more efficiently. This is consistent also with the linear analysis of instability of Eady vortices, published previously (Vic *et al.* 2022).

We have also run simulations, for the same values of B_2/B_1, R_2/R_1 varying R_d/R_1 for the angular mode of perturbation $m = 3$. For $R_d/R_1 = 1$, the growth of the perturbation is slower than that with the angular mode $m = 2$. The linear growth rate of the latter mode is indeed larger than that of $m = 3$ for these vortex parameters. The Eady vortices evolve from a triangular to an elliptical shape and finally break into two hetons. For $R_d/R_1 = 0.5$, the growth rate of mode $m = 3$ is larger than that of mode $m = 2$. In the nonlinear evolution, the vortices form three hetons. For $R_d/R_1 = 0.2$, the vortex breaks on a mode $m = 8$. This confirms the increase of the wavenumber of the most unstable wave as R_d/R_1 decreases. The destabilization of short waves as R_1/R_d increases has also been noticed for the baroclinic instability of vortices in two-layer quasi-geostrophic models (Flierl 1988, Helfrich and Send 1988).

This conclusion also holds for vortices with a hemispheric radial profile of buoyancy, the velocity of which is calculated in the appendix; this buoyancy profile corresponds to a top-hat profile in relative vorticity. For Eady vortices with uniform buoyancy at the two levels, we also observe the same nonlinear regimes using CASL. Therefore our results are generic.

3.1.2. *Study of the hetonic evolution of the unstable Eady vortices*

We next investigate in more detail our reference case $B_2/B_1 = 1$, $R_2/R_1 = 1$, $R_d/R_1 = 1$, $m = 2$. We present in figure 2 the evolution of buoyancy at each level.

The buoyancy patches evolve continuously and simultaneously at the two levels from near disks to ellipses. During their evolution, the angle between them increases to reach approximately $\pi/4$ and does not vary substantially afterwards. The aspect ratio $\lambda = b/a \leq 1$ of the ellipses decreases. Here b and a are the minor and major semi-axis lengths respectively. Further in time, the vortices evolve towards a peanut shape. This shape indicates the presence of higher angular modes of deformation, in particular mode $m = 4$ which is the first harmonic of the fundamental perturbation ($m = 2$). Higher even modes grow non linearly from the interaction of the previous modes; they become important when vortex pinching occurs. The strongly deformed Eady vortices eventually break at their center and form two hetons.

An analysis of the angular modes of deformation, is performed for both levels. We compute the difference between the buoyancy distribution at time t and the initial distribution (considered as nearly axisymmetric because of the weak initial perturbation amplitude). This difference is expressed in polar coordinates:

$$b'_j(r, \theta, t) = b_j(r, \theta, t) - b_j(r, \theta, t = 0),$$

where $j = 1, 2$ is the level index. Then, this difference is expanded in a Fourier series in θ.

$$b'_j(r, \theta, t) = \sum_{m=0}^{\infty} \Re[A_{jm}(r, t) \exp(\mathrm{i}m\theta)],$$

where A_{jm} is the complex amplitude of the angular mode m component of the perturbation on the buoyancy patch at level j. Here we compute the L^2 norm of the modulus of A_{jm} and we present the amplitude $a_{jm}(t)$ with respect to time. This amplitude is calculated via

$$a^2_{jm}(t) = \int_0^L |A_{jm}|^2(r, t)\ r\ dr,$$

where L is large (given by the domain size) so that vortex velocity at this distance is small. Results are shown in figure 3. Clearly, the elliptical component of the deformation grows first, followed in time and in amplitude by the $m = 4$ mode. The antisymmetric mode $m = 1$ and the triangular mode $m = 3$ have a small amplitude.

The ellipticity and the angle of each vortex are determined from the geometric moments of buoyancy (not shown here for brevity). The value obtained confirms that the relative angle between the two vortices is $\pi/4$. This relative orientation of the two vortices maximises the destabilizing influence exerted by each vortex on the other (or, in other words, it maximizes the resonance of unstable Rossby waves on the vortex contours). It must also be noted that the two vortices become irreversibly deformed by acquiring a peanut shape when their aspect ratio is smaller than 0.25. This critical value is reminiscent of that necessary for the breaking of the Kirchhoff elliptical vortex in two-dimensional incompressible fluids ($\lambda = 0.33$).

3.1.3. *A vortex evolution model with a single ellipse*

Considering the similarity between the evolution of our unstable circular Eady vortices, and the evolution of strongly elongated Kirchhoff ellipses, we next study the stationarity and the stability of an elliptical vortex of constant buoyancy depending on its initial aspect ratio.

We perform numerical simulations using a single level SQG model where the buoyancy is confined to a surface, over an infinitely deep ocean/fluid. Specifically, we run simulations for $a/b = 1/\lambda = 3, 4, 5$. Two simulations are run for each case: a short one with a high-frequency temporal sampling to determine the initial rotation rate Ω of the ellipses, and a long one to assess the long-term evolution of each ellipse.

We numerically obtain an estimate for $\Omega \approx \lambda$ for a unit-buoyancy elliptical vortex in the range $3 \leq a/b \leq 5$. It should be noted that the rotation rate of an elliptical vortex with a hemispheric profile of buoyancy has been computed in (Dritschel 2011). The authors showed that indeed Ω is linear in λ in the range $\lambda \in [0, 0.3]$.

Then, we observe that the constant buoyancy elliptical vortex with $\lambda = 1/3$ (or with $\lambda = 1/4$) elongates to a peanut shape but eventually deforms back to an ellipse. In contrast, an elliptical vortex with $\lambda = 1/5$ initially elongates and deforms irreversibly into a peanut-shaped vortex and then breaks into two separate vortices. Again, this indicates that higher modes can grow on an elliptical vortex, during its unsteady, and possibly unstable, evolution; this confirms the angular mode analysis of the unstable circular vortex, presented in subsection 3.1.2.

Figure 4 shows a time series of buoyancy for the elliptical vortex with aspect ratio 1/5. The growth of mode $m = 4$ is clear in the deformation of the ellipse. The growth of this mode, simultaneous with that of mode $m = 2$ is confirmed by a angular mode analysis of the elliptical vortex boundary in time. To achieve this modal analysis, the initial ellipse was subtracted from the instantaneous vortex shape.

As a conclusion, the critical aspect ratio for elliptical SQG vortex breaking (with constant buoyancy) lies in $\lambda \in [0.2, 0.25]$.

We also perform simulations in a two-level SQG model. We initialized identical co-rotating ellipses of constant - but opposite signed - buoyancy at the two levels (with $B_2/B_1 = -1$, $R_2/R_1 = 1$, and with the same aspect ratio).
For $R_d/R_1 = 1$ and $\lambda > 0.2$, the elliptical vortices do not break and they eventually evolve to adopt a steady elliptical shape, as in the one-layer case. For $R_d/R_1 = 0.8$, the elliptical vortices with aspect ratios larger than 0.3 are meta-stable and oscillate around a peanut shape (see panel 2 of figure 3).
In contrast, for $R_d/R_1 = 0.6$, the elliptical vortex breaks for a large range of aspect ratios, namely $\lambda \in [0.3, 0.8]$. Indeed, as H or R_d/R_1 decreases, mode $m = 4$ becomes more linearly unstable, and thus favors vortex breaking (Vic *et al.* 2022). As a conclusion, we note the similarity between our one level model results and those for the Kirchoff ellipse in a two-dimensional fluid. We also note the consistency between the evolution of two-level ellipses and those of the contra-rotating, perturbed, Eady vortices.

3.2. *Nonlinear evolution of Eady vortices with different radii or intensities at the two levels*

Next, we vary the Eady vortex parameters and we classify and explain the unstable evolutions of vertically asymmetric vortices. Figure 5 describes the various nonlinear regimes obtained when varying R_2/R_1 and B_2/B_1, for $R_d/R_1 = 1$ ($H = 1$) and $m = 2$. In the linear stability analysis of such vortices done previously (Vic *et al.* 2022), R_2/R_1 was not varied to keep algebraic equations tractable.

Clearly, the linearly unstable Eady vortex breaks into two hetons when the buoyancy patch radii are identical at both levels. When the bottom vortex patch is smaller and less intense than the surface one, it has a smaller influence on the latter. Therefore, the bottom patch breaks into two symmetric vortices, on each side (horizontally) of the surface patch. This evolution is much slower than that leading to the formation of two hetons. Then, after nonlinear stabilization, the vortex compound thus obtained is called a Λ-tripole, a structure observed previously, in particular in the collision of two oppositely-signed hetons (Reinaud and Carton 2009a, Sokolovskiy and Carton 2010); the formation of a Λ-tripole is illustrated in figure 6. This figure presents a time-series of the buoyancy field, at the surface and bottom. In this case, the surface vortex undergoes a strong elongation and the bottom vortex breaks into two symmetric secondary vortices. After several turn-over periods of the whole structure, the surface vortex relaxes to a less elongated state while the bottom two vortices become its lateral satellites. The whole structure rotates and its ellipticity continues to fluctuate.

The angular mode analysis of the various angular modes is shown for this case on the bottom row of figure 6. It should again, be noted that only even modes grow significantly on each patch. At the surface, mode $m = 2$ grows with superimposed oscillations, a result of the contra-rotation of the two-ellipses. Such an oscillation is also shown in Carton and McWilliams (1996). Mode $m = 4$ grows more slowly but follows the general trend of mode $m = 2$. Both modal amplitudes reach a peak after which they stabilize, decay and oscillate. This peak corresponds to the third panel of figure 6 where the vortex is very elongated. The last stage (stabilisation) corresponds to the relaxation of the vortex towards an ellipse at the surface and to two satellites at the bottom. It should be noted that the bottom perturbation amplitude is weaker, but also that it acts on a weaker vortex. This bottom vortex breaks earlier in the evolution of the whole structure.

When the two patches of the Eady vortex have similar buoyancies, but with a smaller bottom patch, their mutual deformation can become insufficient to break them as hetons. The final outcome of the instability is two contra-rotating elliptical vortices at the two levels (Carton and McWilliams 1996). The formation of contra-rotating ellipses is illustrated in figure 7. This figure presents the surface and bottom maps of buoyancy in the case $R_2/R_1 = 0.5,\ B_2/B_1 = 1,\ R_d/R_1 = 1,\ m = 2$. Clearly the vortex ellipticity initially increases at each level while the vortex rotates. The periodic shear exerted by each vortex on the other level vortex then leads to a pulsating aspect ratio. The bottom vortex, which is smaller, is more deformed.

When varying R_2/R_1 and B_2/B_1, for $H = 0.5$ and $m = 2$, higher modes grow and in particular, when the elliptical mode $m = 2$ is perturbed, its harmonic $m = 4$ grows on the vortex. Both modes are unstable, even if the graver mode is slightly more unstable. Therefore, the final outcome of the nonlinear simulation is usually two hetons, a Λ-tripole or an elliptical vortex, with smaller features due to the growth of mode $m = 4$ (see figure 8).

Further simulations are performed varying R_d/R_1 and B_2/B_1 for $R_1 = R_2$ and $m = 2$. They show the growth of mode $m = 4$ for $R_d = 0.4$, 0.5 and of mode $m = 6$ for $R_d = 0.2$ in agreement with the linear stability analysis of (Vic *et al.* 2022). Simulations are also performed with an initial perturbation of mode $m = 3$. They show the breaking of the unstable vortex into hetons for $R_d/R_1 = 1$, into Λ-tripoles for $R_d/R_1 = 0.5$ and vortex breaking on short unstable waves $m = 6$, 8 for $R_d = 0.2$. Again, this confirms the pre-eminence of short waves for small H. Finally, we added a perturbation with $m = 4$. As predicted by the linear stability analysis (Vic *et al.* 2022), mode $m = 4$ is linearly unstable only for $R_d/R_1 \approx 0.5$. Numerical experiments with the spectral code show that for $R_d/R_1 = 0.7$ to 1, adding a mode $m = 4$ perturbation leads to a transition to a vortex deformation on mode $m = 2$ (which is the subharmonic of $m = 4$, and which is the most unstable linearly), and finally to vortex breaking into two hetons. For $R_d/R_1 = 0.5$, vortex breaking occurs on $m = 4$ and forms 4 hetons. For $R_d/R_1 = 0.6$, a complex wave interaction occurs and the final result is asymmetric.

3.2.1. *Influence of a horizontal offset between the vortex centers*

We briefly report on the influence of a finite horizontal distance between the vortex centers. If the two centers are far apart, the effect of one disk of buoyancy on the other is comparable with that of a point vortex. It is known that the far velocity field of a vortex is an advection and a deformation. In this deformation field, the mode 2 component (with respect to the deformed vortex center) has a larger amplitude than that of mode 3, and further on for higher modes. Therefore we expect the horizontal offset to:
1) create a hetonic coupling when the two vortices are far apart (i.e. couple the surface and bottom vortex patches as a baroclinic dipole which translates perpendicularly to the dipole axis)
2) favor both mode 1 and 2 deformation for closer vortices,
3) contribute to the growth of even higher modes of deformation (modes 3 and 4) for very close vortices.

After this physical analysis, we turn to numerical experiments where we vary the distance d between the vortex patch centers, for given R_d/R_1, R_2/R_1, B_2/B_1.
Firstly, we set $R_d/R_1 = 1, R_2/R_1 = 1, B_2/B_1 = 1$. While for $d = 0$, the breaking of the vortex into two hetons is symmetrical, it becomes increasing asymetric as d increases. However, for $d = 0.9$, the vortices do not break but form a heton. This illustrates the transition between hetonic coupling of two widely offset vortices and baroclinic instability of a slightly tilted contra-rotating vortex (Polvani *et al.* 1989, Dritschel 1995).
Secondly, we set $R_d/R_1 = 1, R_2/R_1 = 0.5, B_2/B_1 = 1$. A similar result is obtained. For $d = 0$, a dipolar breaking of each vortex occurs, leading to the formation of two hetons. In contrast, for $d = 1$, the surface and bottom vortices pair to form a single heton without breaking. Finally, we set $R_d/R_1 = 0.5, R_2/R_1 = 1, B_2/B_1 = 1$. We recall that for $d = 0$, the vortex patches undergo a mode $m = 4$ deformation. As d grows, the single heton which forms and moves away from the plane center, leaves behind fewer and fewer fragments.

3.3. *A model of the Λ-tripole with three vortices on two levels*

We next show that an initial aggregate of three buoyancy patches, one at the center of the fluid surface, two laterally shifted at the bottom of the fluid, can adjust nonlinearly to form a Λ-tripole. We run a simulation with $B_2/B_1 = 0.5$, $R_2/R_1 = 0.5$, $R_d/R_1 = 1$, $d = 4R_2$ starting from three circular patches. Here d is the distance between the centers of the two patches. Figure 9 shows that each patch deforms under the influence of the other two patches, and in particular, elongates. The surface patch finally adjusts to an ellipse. The bottom satellite vortices then lie along the surface vortex boundary.

4. Evolution of two offset, co-rotating Eady vortices, with opposite-signed buoyancy anomalies

In this section, we assess the robustness of a co-rotating Eady vortex, with opposite-signed buoyancy anomalies at the two levels ($B_2/B_1 < 0$). More specifically, we study the ability of such a vortex, initially tilted, to straighten up. This process is important in geophysical fluids. In the ocean or in the atmosphere, drifting vortices are affected by a perturbation with horizontal mode $m = 1$. This perturbation leads to the tilting of the vortex with respect to the vertical axis. The robustness of tilted vortices is therefore an important questions. Again, for simplicity, we consider vortices with uniform buoyancy at each level. Initially, we offset the surface and bottom patches horizontally, by a distance d.

Figure 10 shows the evolution of tilted vortices with $R_2/R_1 = 1$, $B_2/B_1 = -1$, for various values of R_d/R_1 and of the relative horizontal offset d/R_1. The nonlinear evolutions are either towards the vertical alignment of the vortices, or their co-rotation around a central axis with the absence of convergence of the two patches towards the center.

For $R_d/R_1 \leq 1.0$, vertical alignment occurs for vortices initially distant of 3.3 vortex radii or less. When vortices are initially farther away, they simply rotate around the center of the plane. Note that this critical distance $d/R_1 = 3.3$ is close to the critical distance for the merger of two vortices, with uniform vorticity, in two-dimensional incompressible flows (Melander *et al.* 1988). It is also the critical distance for the merger of two vortices in a two-layer (internal) quasi-geostrophic model, when the vortices are confined at the fluid surface (Polvani *et al.* 1989).
When R_d/R_1 is increased beyond 1, the critical distance for alignment decreases rapidly. For $R_d/R_1 = 1.25$ it is less than 3. For $R_d/R_1 = 1.4$, no complete alignment is observed anymore. Only a moderate convergence of the two patches occurs. Their separation decreases by half and then oscillates. The vortices mostly co-rotate. For $R_d/R_1 = 1.5$, only a weak (partial) convergence followed by a weak radial oscillation, accompanies the co-rotation of the two vortices. Finally, for $R_d/R_1 \geq 2$, only co-rotation is observed.

Our regime diagram is similar to the one of Polvani (1991) (his figure 7) for the alignment of two-layer, internal quasi-geostrophic vortices. The critical value for alignment is also $d/R \approx 3.3$ and the maximal value of $1/\gamma$ (the equivalent of H in our study) is unity. It should be noted also that, for very small d/R initially, alignment is replaced by partial convergence.

The final state of the vortex depends on H. Various cases are shown below.
Firstly, for $B_2/B_1 = -1$, $R_2/R_1 = 1$, $R_d/R_1 = 1$, $d = 1$, alignment occurs. Figure 11 shows time series of buoyancy maps. The two patches overlap increasingly with time. To ensure conservation of angular momentum, the vortex sheds filaments which wrap around the final vortex. The interaction of the central vortex with the peripheral vorticity supports vortex contour waves (vortex Rossby waves) which induce a phase shift between the two vortices. This explains why the inter-centroid distance oscillates while decreasing with time.

Figure 12 shows that, initially, the streamlines and the buoyancy isolines do not coincide (the fluid surface is shown here; the situation is symmetric at the bottom). This indicates that the buoyancy field is unsteady and that buoyancy is advected towards the center of the plane (as shown by the streamlines). At the end of the simulation (same figure), the buoyancy distribution is not steady yet but the streamlines match the buoyancy contours better. A longer simulation would be necessary to attain full stationarity, if any.
In contrast, for $B_2/B_1 = -1$, $R_2/R_1 = 1$, $R_d/R_1 = 1$, $d = 4$, co-rotation occurs. Figure 13

shows time series of buoyancy maps. Clearly, each vortex rotates around the center of the plane, as shown by the inter-centroid distance, which only varies little. The mutual influence of the two vortices is manifested by the Rossby waves on the vortex boundaries. As it appears in this figure, low modes of deformation grow first (modes 1 and 2, leading to a slightly asymmetric ellipse for the vortex contours). Then higher modes grow by nonlinear interaction: this is seen on the last buoyancy map of figure 13 where a mode $m = 4$ deformation of the vortices appears. Nevertheless, this contour deformation never leads the vortices to deform so much to overlap near the center of the plane. Vertical alignment does not occur.

Finally, the regimes of weak to moderate convergence, with oscillation, lie in between the previous two regimes. The time variation of the inter-centroid distance increases from co-rotation, to weak to moderate convergence and finally to vertical alignment. The amplitude of contour deformation also increases. The combination of the two effects favor alignment.

5. Discussion

Our numerical experiments yield the following results:

- for like-signed buoyancy at the surface and bottom, contra-rotating Eady vortices undergo baroclinic instability for increasing angular wavenumbers as the fluid height decreases. Low wavenumber ($m = 2, 3$) perturbations lead to hetonic breaking when the two level buoyancy patches have comparable size and strength. In contrast, for vertically asymmetric vortices, vortex elliptisation or the formation of Λ-tripoles, are observed.
- The formation of a Λ-tripole results from a nonlinear equilibration of the linearly unstable contra-rotating Eady vortex. Higher wavenumber perturbations saturate at finite amplitude, in particular for mode $m = 4$. It is also shown that a Λ-tripole is an attractor for nearby states: three vortices initialised in this configuration, but with a circular shape, deform until they reach the configuration observed in the nonlinear experiments of baroclinic vortex instability.
- For opposite-signed buoyancies at the surface and bottom (co-rotating vortices), vertical alignment can occur when the total height of the fluid is smaller than, or equal to unity, and when the initial horizontal distance between the two vortices is smaller than, or equal to, three vortex radii. Unequal vortices have not been considered here.
- In both alignment and co-rotation regimes, vortex Rossby waves are observed. In the alignment regime, they participate in the overlapping of buoyancy, and to he appearance of a mode $m = 1$ deformation (corresponding to a dipolar effect), eventually leading to the convergence of vortices towards the center of the plane.
- Intermediate regimes, between the former two regimes, exist, exhibiting radial oscillations at various degrees. They occur more specifically for larger fluid heights (vertically more separated buoyancy levels).

These results confirm and extend those previously obtained with a two-layer (internal) quasi-geostrophic model: in particular for baroclinic vortex instability (Flierl 1988, Helfrich and Send 1988). Clear analogies exist in the nonlinear evolutions, in particular the existence of nonlinearly equilibrated states for linearly unstable vortices, or the possible breaking of linearly unstable vortices into hetons. Similarly, previous studies found that vortices with like-signed potential vorticity could align in a two-layer quasi-geostrophic model if the vortices were large and close enough initially (Polvani 1991). These similarities can be related to the similarity between the Phillips and Eady models of baroclinic instability of jets (Eady 1949, Phillips 1954). Nevertheless, the SQG model produces more fine-scale features (filaments) and also leads to higher vertical velocities as described in Lapeyre (2017). This is important in

particular for near surface dynamics. Smith and Bernard (2013) noted that the SQG model can apply to a depth with a rapid change in stratification. This is the case of the base of the oceanic mixed layer. The internal quasi-geostrophic model, on the contrary, pertains to deeper vortices. Despite this, results from the two models concerning the baroclinic instability of vortices, or their ability to align vertically, are quite similar.

6. Conclusion

Our study extends those on vortex barotropic instability in surface quasi-geostrophic dynamics. They provide results comparable to those of vortex studies in internal quasi-geostrophic models, but for shallower vortices. Naturally, this study should be extended to ageostrophic dynamics (either in a two-level SQG^{+1} model, which is an extension of the SQG model (Hakim *et al.* 2002), or in a fully stratified, primitive equation, model). Oceanic vortices have complex vertical structures, and, when deformed, they are associated with finite vertical velocities. Complex three-dimensional motions and vortex structures are not included in the present study. Using a primitive equation model (3D hydrostatic model) will substantially extend our results, via the inclusion of high frequency components of velocity and by allowing ageostrophic instabilities to occur.

Concerning observations at sea, new measurement devices (tow-yo, gliders) allow repeated measurements of interacting vortices at the submesoscale (McWilliams 1985, Chavanne *et al.* 2010, Bosse *et al.* 2016). Very high resolution numerical models also show evidence of such processes (Gula *et al.* 2015, Morvan *et al.* 2019). Such interactions were proved to strengthen these small vortices against the decay due to ambient shear and strain effects, turbulent diffusion, Rossby wave dispersion or topographic interactions, and thus make submesoscale eddies more robust. In particular it is important to quantify the efficiency of vortex alignment and vortex merger, in three-dimensional ocean dynamics, when the vortices are not isolated. Our study is only a step towards this goal. Further studies will include more physical effects (in 3D stratified rotating dynamics), but should retain few physical parameters to remain numerically tractable. The quantification of 3D vortex interactions will refine assessments of the contribution of oceanic eddies to heat and salt transport at large scale.

Appendix A:

Here we calculate the streamfunction associated with a hemispheric radial distribution of buoyancy for a two-level SQG vortex :

$$B^s = B_0^s\sqrt{1-r^2}\ \mathrm{He}(1-r), \qquad B^b = B_0^b\sqrt{1-r^2}\ \mathrm{He}(1-r), \tag{A.1}$$

where He is the Heaviside function $\mathrm{He}(x) = 1$ if $x \geq 0$ and $\mathrm{He}(x) = 0$ if $x < 0$. The angular velocity of a single vortex defined by this steady state is drawn in Figure A1.

Indeed, for any buoyancy b^s or b^b (Vic *et al.* 2022) (where s stands for surface and b for bottom):

$$\psi^s(r,\phi,z=0,t) = \sum_{n\in N}\int_0^\infty \frac{J_n(\rho r)}{\sigma\sinh(\rho\sigma)}\left(\widehat{b^b} - \widehat{b^s}\cosh(\rho\sigma)\right)\mathrm{d}\rho\ \exp(\mathrm{i}n\phi),$$

$$\psi^b(r,\phi,z=1,t) = \sum_{n\in N}\int_0^\infty \frac{J_n(\rho r)}{\sigma\sinh(\rho\sigma)}\left(\widehat{b^b}\cosh(\rho\sigma) - \widehat{b^s}\right)\mathrm{d}\rho\ \exp(\mathrm{i}n\phi), \tag{A.2}$$

where $\sigma = N_0 H/f_0$.

Computing the streamfunction of the steady state requires the Fourier transforms of the steady state buoyancies: for $\rho > 0$ and $n \in Z^*$:

$$\widehat{B^s}(\rho, n) = \frac{B_0^s}{2\pi} \int_0^{2\pi} \int_0^1 \sqrt{1-r^2}\ J_n(\rho r)\ r\ \exp(-\mathrm{in}\phi\ \mathrm{dr}\ \mathrm{d}\phi = 0. \tag{A.3}$$

For $n = 0$, posing $r = \sin\alpha$, using formula 11.4.10. from (Abramowitz and Stegun 1964) and the equality

$$J_{3/2}(x) = \sqrt{\frac{2}{\pi}} \frac{\sin x - x\cos x}{x^{3/2}},$$

we have:

$$\widehat{B^s}(\rho, 0) = B_0^s \int_0^1 \sqrt{1-r^2} J_0(\rho r)\ r\ \mathrm{d}r, \tag{A.4}$$

$$= B_0^s \int_0^{\pi/2} \cos^2\alpha \sin\alpha\ J_0(\rho\sin\alpha)\mathrm{d}\alpha, \tag{A.5}$$

$$= B_0^s \sqrt{2}\ \Gamma\left(\frac{3}{2}\right) \frac{J_{3/2}(\rho)}{\rho^{3/2}}, \tag{A.6}$$

$$= B_0^s \sqrt{\frac{\pi}{2}}\ \frac{J_{3/2}(\rho)}{\rho^{3/2}}, \tag{A.7}$$

$$\widehat{B^s}(\rho, 0) = B_0^s \frac{\sin\rho - \rho\cos\rho}{\rho^3}, \tag{A.8}$$

and similarly for

$$\widehat{B^b}(\rho, 0) = B_0^b \frac{\sin\rho - \rho\cos\rho}{\rho^3}. \tag{A.9}$$

From these identities, the steady state streamfunction at the two levels are:

$$\Psi^s(r, \phi, z = 0, t) = \int_0^\infty \frac{J_0(\rho r)}{\sigma\sinh(\rho\sigma)}\ \frac{\sin\rho - \rho\cos\rho}{\rho^3} \left(B_0^b - B_0^s\cosh(\rho\sigma)\right) \mathrm{d}\rho, \tag{A.10a}$$

$$\Psi^b(r, \phi, z = 1, t) = \int_0^\infty \frac{J_0(\rho r)}{\sigma\sinh(\rho\sigma)} \frac{\sin\rho - \rho\cos\rho}{\rho^3} \left(B_0^b\cosh(\rho\sigma) - B_0^s\right) \mathrm{d}\rho. \tag{A.10b}$$

The steady state velocity field is plotted in figure A1: the radial velocities are null because the streamfunctions have no angular component and $U_\phi = \dfrac{\mathrm{d}\Psi}{\mathrm{d}r}$ so :

$$U_\phi^s = B_0^b E_1(r, \sigma) + B_0^s F_1(r, \sigma), \tag{A.11a}$$

$$U_\phi^b = B_0^b F_1(r, \sigma) + B_0^s E_1(r, \sigma), \tag{A.11b}$$

where the function E_1 and F_1 are defined by the following integrals (and drawn in Figure A2):

$$E_1(r, \sigma) = \int_0^\infty \frac{J_1(\rho r)}{\sigma\sinh(\rho\sigma)} \frac{\rho\cos\rho - \sin\rho}{\rho^2} \mathrm{d}\rho, \tag{A.12a}$$

$$F_1(r, \sigma) = \int_0^\infty \frac{J_1(\rho r)}{\sigma\tanh(\rho\sigma)} \frac{\rho\cos\rho - \sin\rho}{\rho^2} \mathrm{d}\rho. \tag{A.12b}$$

References

Abramowitz, M. and Stegun, I., *Handbook of mathematical functions with formulas, graphs et mathematical tables*, Vol. Applied Mathematics Series 55, 1964 (National Bureau of Standards).

Badin, G. and Poulin, F.J., Asymptotic scale-dependent stability of surface quasi-geostrophic vortices: semi-analytic results. *Geophys. Astrophys. Fluid Dyn.*, 2019, **113**, 574–593.

Baey, J.M. and Carton, X., Vortex multipoles in two-layer rotating shallow-water flows. *J. Fluid Mech.*, 2002, pp. 151–175.

Bosse, A., Testor, P., Houpert, L., Damien, P., Prieur, L., Hayes, D., Taillandier, V., Durrieu de Madron, X., d'Ortenzio, F., Coppola, L., Karstensen, J. and Mortier, L., Scales and dynamics of Submesoscale Coherent Vortices formed by deep convection in the northwestern Mediterranean Sea. *J. Geophys. Res.: Oceans*, 2016, **121**, 7716–7742.

Bretherton, F.P., Critical layer instability in baroclinic flows. *Q. J. R. Meteorol. Soc.*, 1966, **92**, 325–334.

Carton, X., Instability of Surface Quasigeostrophic Vortices. *J. Atmosp. Sci.*, 2009, **66**, 1051–1062.

Carton, X., Flierl, G.R., Perrot, X., Meunier, T. and Sokolovskiy, M.A., Explosive instability of geostrophic vortices. Part 1: baroclinic instability. *Theor. comput. fluid dyn.*, 2010, **24**, 125–130.

Carton, X.J. and McWilliams, J.C., Nonlinear oscillatory evolution of a baroclinically unstable geostrophic vortex. *Dyn. Atmos. Oceans*, 1996, pp. 207–214.

Carton, X.J., Poulin, F.P. and Pavec, M., Linear baroclinic and parametric instabilities of boundary currents. *Geophys. Astrophys. Fluid Dyn.*, 2011, **105**, 453–477.

Charney, J.G., On the scale of atmospheric motions. *Geofys. Publik.*, 1948, pp. 1–17.

Chavanne, C., Flament, P. and Gurgel, K.W., Interactions between a Submesoscale Anticyclonic Vortex and a Front. *J. Phys. Oceanogr.*, 2010, **40**.

Dritschel, D.G., An exact, steadily rotating surface quasi-geostrophic elliptical vortex. *Geophys. Astrophys. Fluid Dyn.*, 2011, **105**, 368–376.

Dritschel, D., A general theory for two-dimensional vortex interactions.. *J. Fluid Mech.*, 1995, **293**, 269–303.

Eady, E.T., Long Waves and Cyclone Waves. *Tellus*, 1949, **1**, 33–52.

Flierl, G.R., Models of vertical structure and the calibration of two-layer models. *Dyn. Atmos. Oceans*, 1978, **2**, 341–381.

Flierl, G.R., On the instability of geostrophic vortices. *J. Fluid Mech.*, 1988, pp. 349–388.

Gryanik, V.M., Dynamics of singular geostrophic vortices in a two-level model of the atmosphere (or ocean). *Izv. Akad. Nauk. SSSR, Atmos. Ocean. Phys.*, 1983, **19**, 171–179.

Gula, J., Molemaker, M.J. and McWilliams, J.C., Topographic vorticity generation, submesoscale instability and vortex street formation in the Gulf Stream. *Geophys. Res. Lett.*, 2015, **42**, 4054–4062.

Gula, J., Blacic, T.M. and Todd, R.E., Submesoscale Coherent Vortices in the Gulf Stream. *Geophys. Res. Lett.*, 2019, **46**, 1–11.

Gula, J., Taylor, J., Scherbina, A. and Mahadevan, A., Submesoscale processes and mixing; in *Ocean Mixing*, Vol. chapter 8, 2022, pp. 181–214.

Hakim, G., Snyder, C. and Muraki, D., A New Surface Model for Cyclone–Anticyclone Asymmetry. *J. Atmos. Sci.*, 2002, **59**, 2405 – 2420.

Harvey, B.J. and Ambaum, M.H.P., Perturbed Rankine vortices in surface quasi-geostrophic dynamics. *Geophys. Astrophys. Fluid Dyn.*, 2011, **105**, 377–391.

Harvey, B.J., Ambaum, M.H.P. and Carton, X., Instability of shielded surface temperature vortices. *J. Atmos. Sci.*, 2011, **68**, 964–971.

Held, I., PierreHumbert, R.T., Garner, S.T. and Swanson, K.L., Surface quasi-geostrophic dynamics. *J. Fluid Mech.*, 1995, pp. 1–20.

Helfrich, K. and Send, U., Finite-amplitude evolution of two-layer geostrophic vortices. *J. Fluid Mech.*, 1988, pp. 331–348.

Hogg, N.G. and Stommel, H.M., The heton, an elementary interaction between discrete baroclinic geostrophic vortices, and its implications concerning eddy heat-flow. *Proc. R. Soc. London A*, 1985a, **397**, 1–20.

Hogg, N.G. and Stommel, H.M., Hetonic Explosions: The Breakup and Spread of Warm Pools as Explained by Baroclinic Point Vortices. *J. Atmos. Sci.*, 1985b, **42**, 1465–1476.

Klein, P., Hua, B.L., Lapeyre, G., Capet, X., Le Gentil, S. and Sasaki, H., Upper Ocean Turbulence from High-Resolution 3D Simulations. *J. Phys. Oceanogr.*, 2008, **38**, 1748–1763.

Lapeyre, G. and Klein, P., Dynamics of the Upper Oceanic Layers in Terms of Surface Quasigeostrophy Theory. *J. Phys. Oceanogr.*, 2006, **36**, 165–176.

Lapeyre, G., Surface Quasi-Geostrophy. *Fluids*, 2017, **2**, 1–28.

McWilliams, J.C., Submesoscale, coherent vortices in the ocean. *Rev. Geophys.*, 1985, **23**, 165–182.

McWilliams, J.C., Geostrophic Vortices; in , 1991, pp. 5–50.

Melander, M.V., Zabusky, N.J. and McWilliams, J.C., Symmetric vortex merger in two dimensions - Causes and conditions. *J. Fluid Mech.*, 1988, **195**, 303–340.

Morvan, M., L'Hégaret, P., Carton, X., Gula, J., Vic, C., de Marez, C., Sokolovskiy, M. and Koshel, K., The life cycle of submesoscale eddies generated by topographic interactions. *Ocean Sci.*, 2019, **15**, 1531–1543.

Oulhen, E., Reinaud, J. and Carton, X., Formation of small scale vortices in the core of a large merged vortex. *Geophys. Astrophys. Fluid Dyn.*, 2022, **116**, 411–432.

Perrot, X., Reinaud, J., Carton, X. and Dritschel, D., Homostrophic vortex interaction in a coupled QG-SQG

model. *Reg. Chaotic Dyn.*, 2010, **15**, 67–84.

Phillips, N.A., Energy Transformations and Meridional Circulations associated with simple Baroclinic Waves in a two-level, Quasi-geostrophic Model. *Tellus*, 1954, **6**, 274–286.

Polvani, L., Two-layer geostrophic vortex dynamics. Part 2. Alignment and two-layer V-states. *J. Fluid Mech.*, 1991, **225**, 241–270.

Polvani, L.M., Zabusky, N.J. and Flierl, G.R., Two-layer geostrophic vortex dynamics. Part 1. Upper-layer V-states and merger. *J. Fluid Mech.*, 1989, **205**, 215–242.

Provenzale, A., Transport by coherent barotropic vortices. *Ann. Rev. Fluid Mech.*, 1999, **31**, 55–93.

Reinaud, J., Three-dimensional quasi-geostrophic vortex equilibria with m-fold symmetry. *J. Fluid Mech.*, 2019, **863**, 32–59.

Reinaud, J.N. and Carton, X.J., Existence, stability and formation of baroclinic tripoles in quasi-geostrophic flows. *J. Fluid Mech.*, 2009a, **785**, 1–30.

Reinaud, J.N. and Carton, X.J., The stability and the nonlinear evolution of quasi-geostrophic hetons. *J. Fluid Mech.*, 2009b, **636**, 109–135.

Reinaud, J.N., Dritschel, D.G. and Scott, R.K., Self-similar collapse of three vortices in the generalised Euler and quasi-geostrophic equations. *Phys. D: Nonlinear Phenom.*, 2022, **434**.

Reinaud, J., Dritschel, D. and Carton, X., Interaction between a surface quasi-geostrophic buoyancy anomaly strip and an internal vortex. *Geophys. Astrophys. Fluid Dyn.*, 2016, **110**, 461–490.

Reinaud, J., Dritschel, D. and Carton, X., Interaction between a quasi-geostrophic buoyancy filament and a heton. *Fluids*, 2017a, **2**, 37.

Reinaud, J., Dritschel, D. and Carton, X., Interaction between a surface quasi-geostrophic buoyancy anomaly jet and internal vortices. *Phys. Fluids*, 2017b, **29**.

Richardson, P.L., Gulf-Stream rings; in *Eddies in Marine Science*, edited by A.R. Robinson, Vol. Topics in Atmospheric and Oceanographic Sciences, 1983, pp. 19–45.

Smith, K.S. and Bernard, E., Geostrophic turbulence near rapid changes in stratification. *Phys. Fluids*, 2013, **25**, 046601.

Sokolovskiy, M.A. and Carton, X.J., Baroclinic multipole formation from heton interaction. *Fluid Dyn. Res.*, 2010, **42**.

Sokolovskiy, M.A. and Verron, J., *Dynamics of Vortex Structures in a Stratified Rotating Fluid*, 2013 (Springer).

Tulloch, R. and Smith, K.S., Quasigeostrophic Turbulence with Explicit Surface Dynamics: Application to the Atmospheric Energy Spectrum. *J. Atmos. Sci.*, 2009, **66**, 450–467.

Vic, A., Carton, X. and Gula, J., Eady baroclinic instability of a circular vortex. *Symmetry*, 2022, **14**, 1–18.

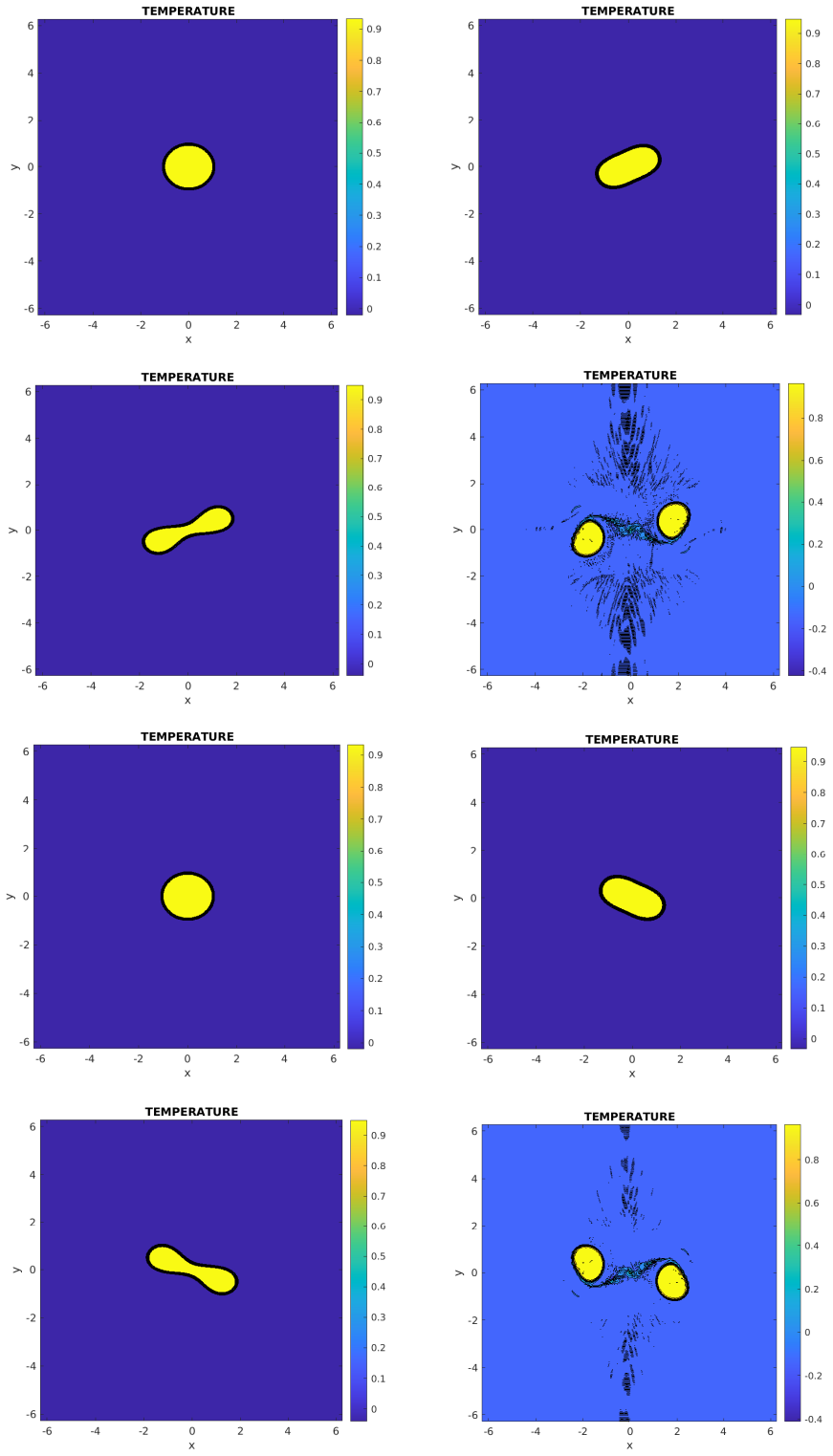

Figure 2. Hetonic breaking of an unstable contra-rotating Eady vortex with uniform buoyancy at the two levels; time-series of horizontal maps of buoyancy; the parameters are $B_2/B_1 = 1$, $R_2/R_1 = 1$, $R_d/R_1 = 1$, $m = 2$. The upper two rows show the surface buoyancy evolution, and the lower two rows, the bottom buoyancy. For each level, frames are read from left to right and then from top to bottom. Times shown are $0, 8, 12, 20$ model time units (Colour online).

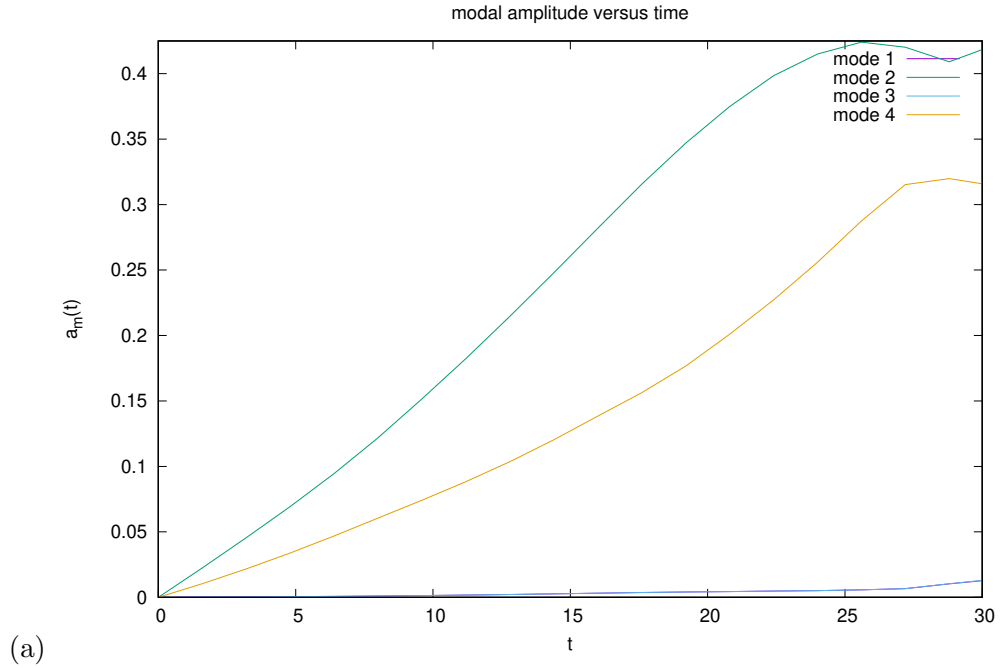

(a)

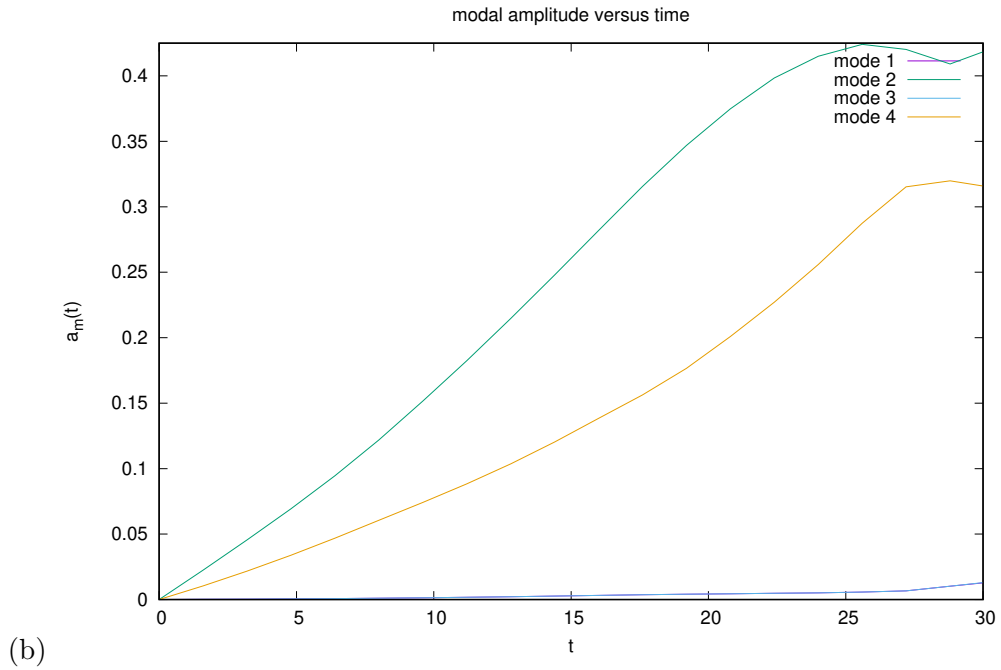

(b)

Figure 3. Angular mode analysis of the hetonic breaking of an unstable contra-rotating Eady vortex with uniform buoyancy at each level (see the text for their definition); the parameters are $B_2/B_1 = 1$, $R_2/R_1 = 1$, $R_d/R_1 = 1$, $m = 2$. The amplitudes of the various angular modes are shown, the modes are $m = 1$, 2, 3, 4. (a): surface vortex modes; (b): bottom vortex modes (Colour online).

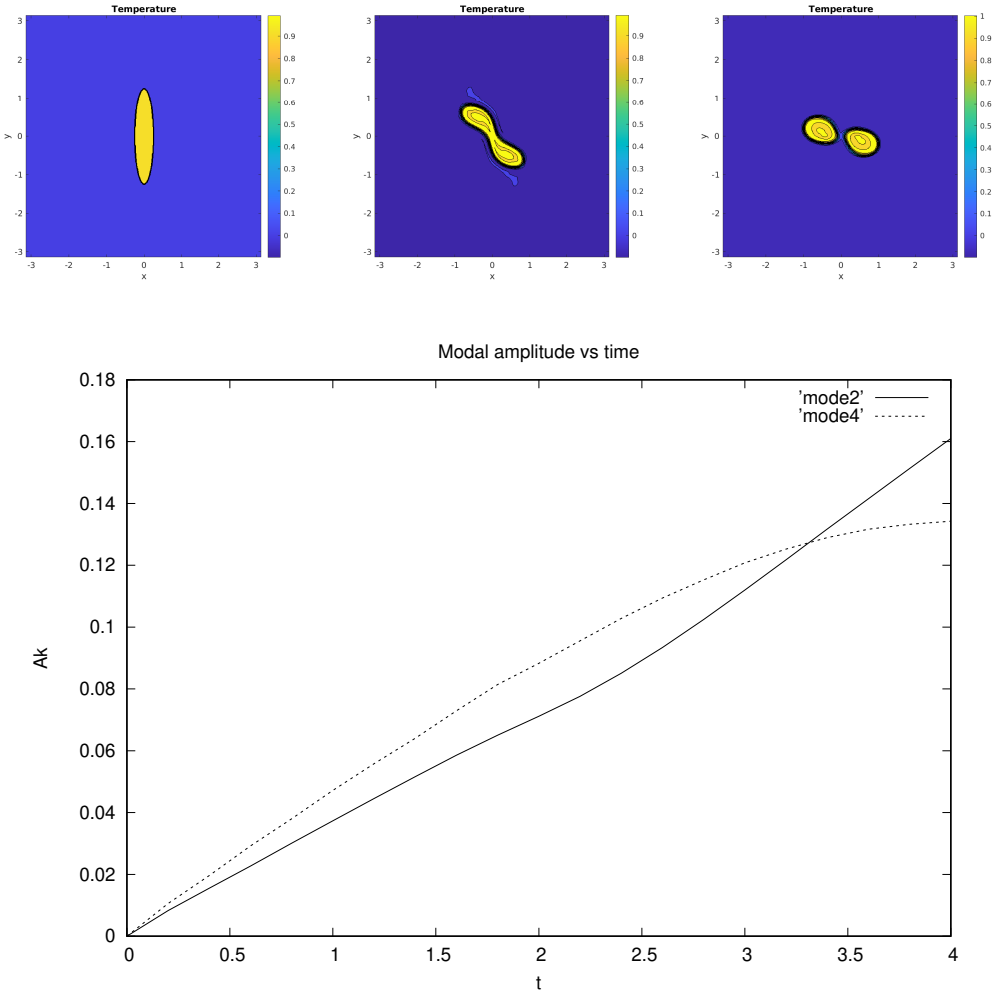

Figure 4. Top : Time series of horizontal maps of buoyancy showing the nonlinear breaking of an elliptical vortex, with uniform buoyancy, in a vertically semi infinite fluid; the aspect ratio of the ellipse is $b/a = 1/5$ initially. Times shown are $t = 0$, 4, 8 from left to right. Bottom: Modal analysis of the one-level SQG ellipse with uniform buoyancy. The two angular modes shown are $m = 2$, 4. For $m = 2$ the initial value was subtracted (Colour online).

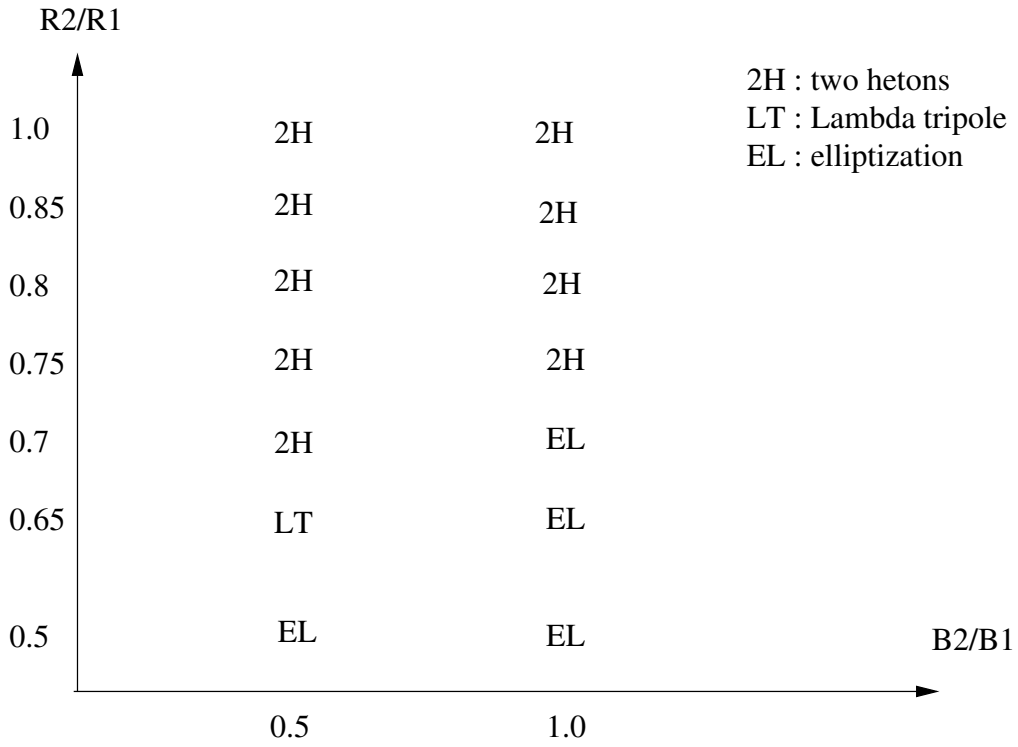

Figure 5. Nonlinear regimes of the unstable contra-rotating Eady vortex, with respect to the buoyancy patch radii and magnitudes, for $B_1 = 1$, $R_1 = 1$, $H = 1$, $m = 2$.

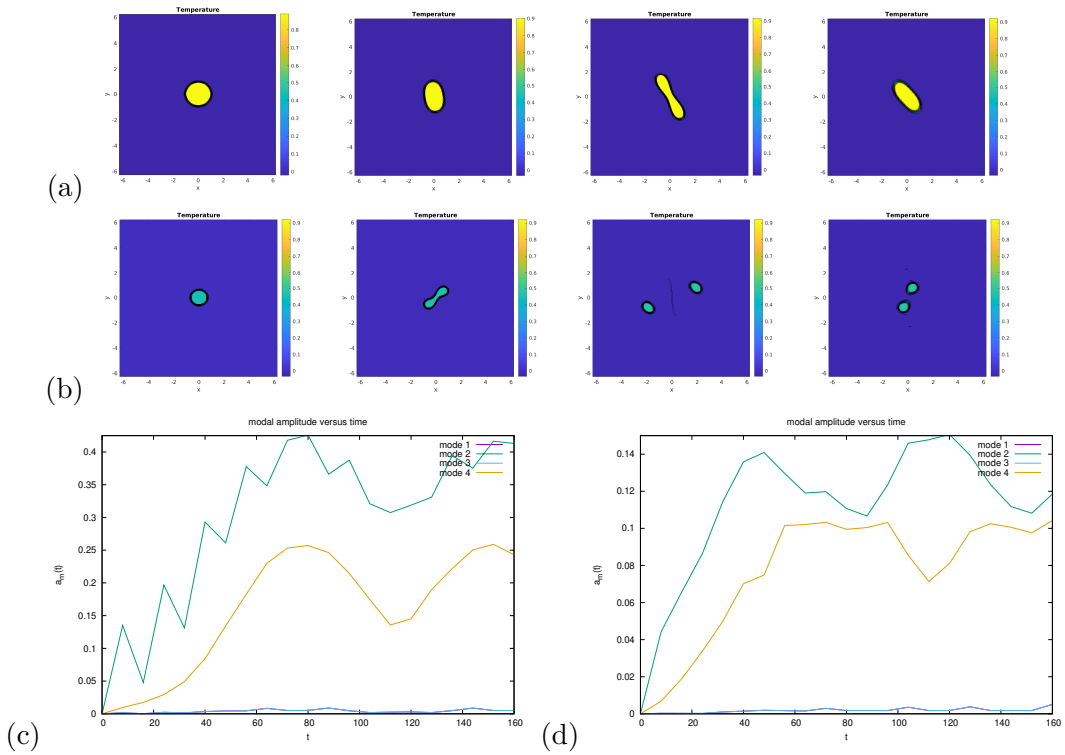

Figure 6. Λ-tripole formation from the nonlinear evolution of an unstable contra-rotating Eady vortex with uniform buoyancy; time-series of horizontal maps of buoyancy. The upper row (a) shows the surface buoyancy, and the middle row (b), the bottom buoyancy. Times shown are 0, 48, 72, 120 model time units. The bottom row (c,d) shows the angular mode analysis of the unstable contra-rotating Eady vortex forming a Λ-tripole; the parameters are $B_2/B_1 = 0.5$, $R_2/R_1 = 0.65$, $R_d/R_1 = 1$, $m = 2$. The various angular modes shown are $m = 1$, 2, 3, 4. Left panel (c): modes of the surface vortex; right panel (d): modes of the bottom vortex (Colour online).

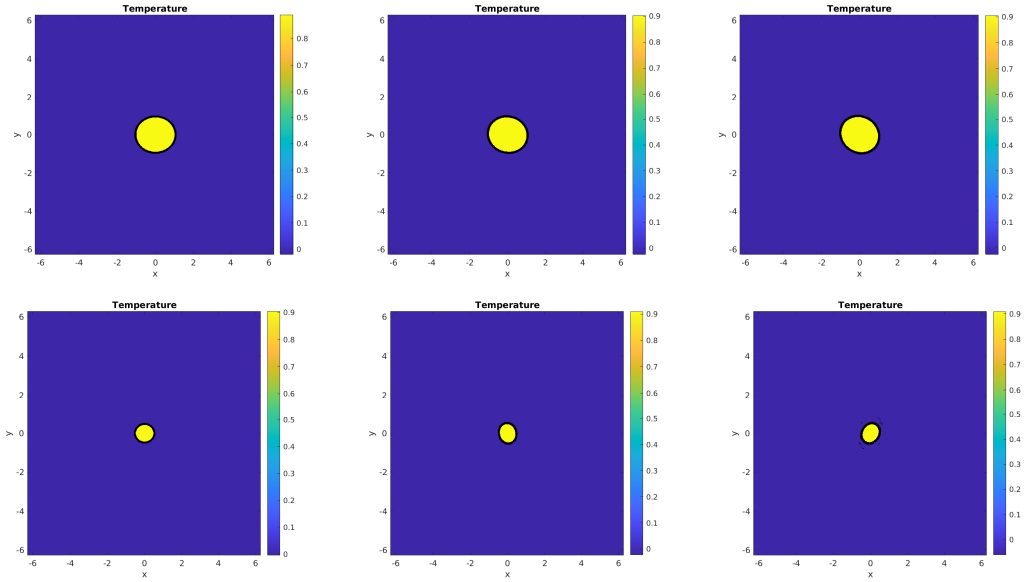

Figure 7. Nonlinear evolution of an unstable contra-rotating Eady vortex with uniform buoyancy in a disk; the parameters are $B_2/B_1 = 1$, $R_2/R_1 = 0.5$, $R_1/R_d = 1$, $m = 2$. The upper row shows the surface buoyancy, and the lower row, the bottom buoyancy. Times shown are $0, 90, 180$ model time units (Colour online).

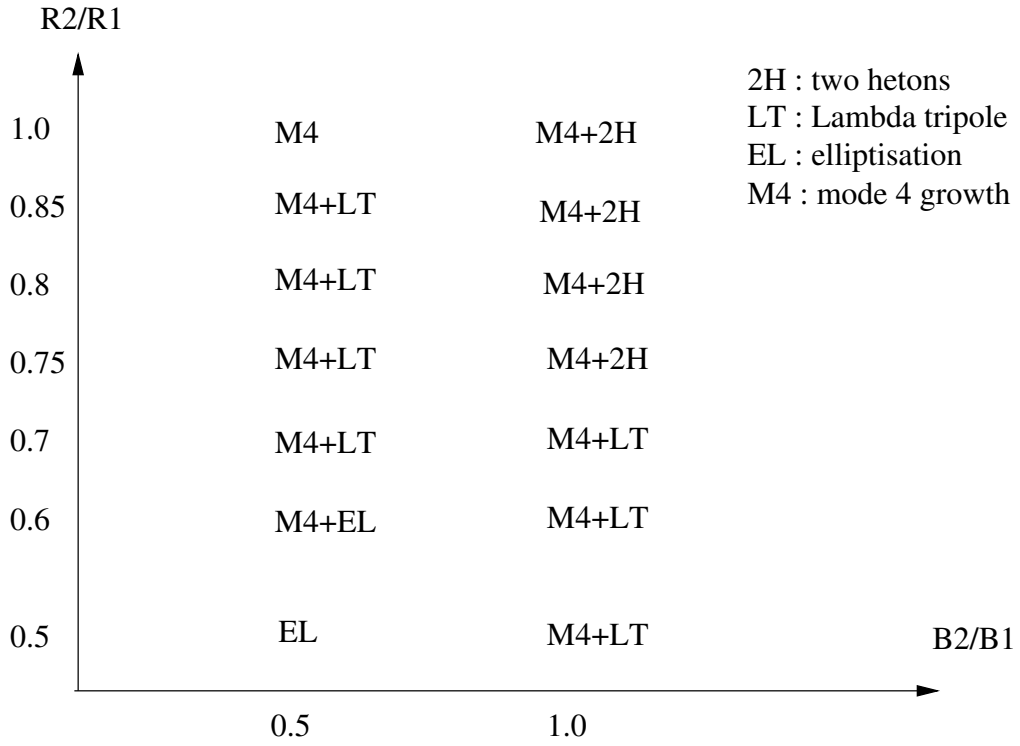

Figure 8. Nonlinear regimes of the unstable contra-rotating Eady vortex, with respect to the patch radii and buoyancies, for $B_1 = 1$, $R_1 = 1$, $R_1 = 2R_d$ ($H = 0.5$), $m = 2$.

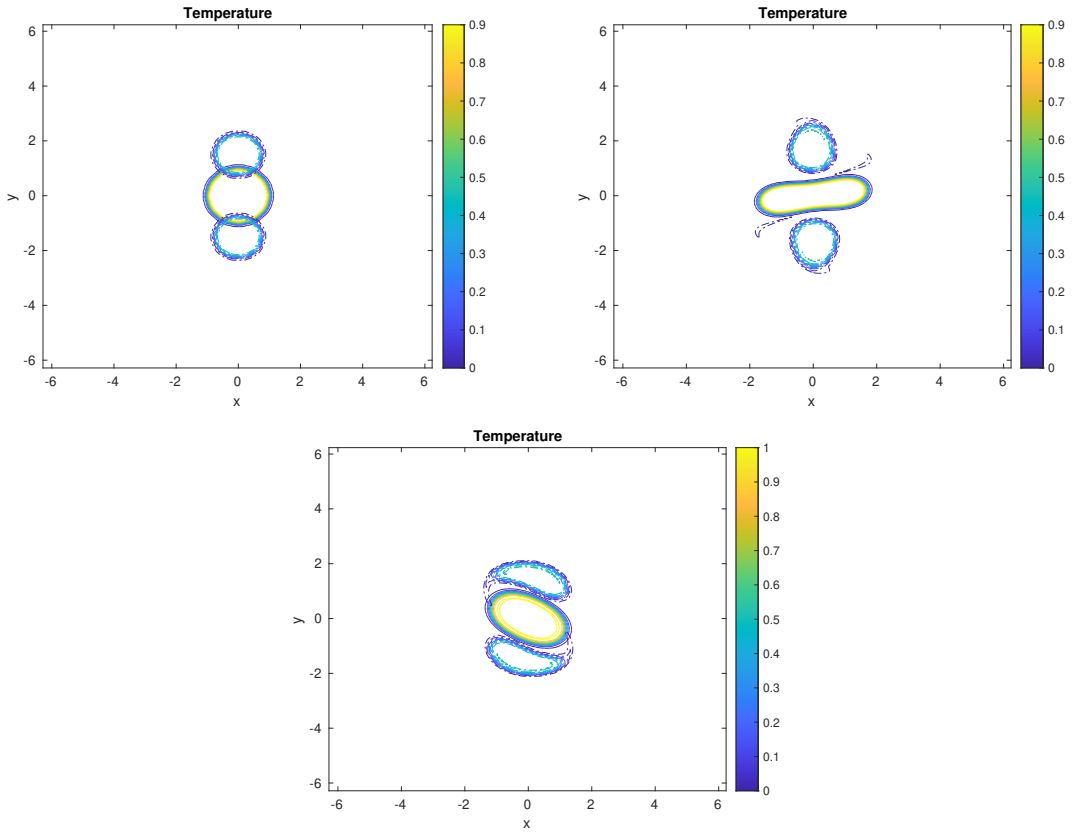

Figure 9. Time series of buoyancy maps for the surface (solid lines) and the bottom (dashed lines) superimposed, showing the evolution of a vortex aggregate towards a Lambda tripole. Times shown are t=0, 28, 42 model time units. The vortex parameters are $B_1 = 1, B_2 = 0.5$, $R_1 = 1, R_2 = 0.5$, $H = R_d = 1$, $d = 4R_2$ (Colour online).

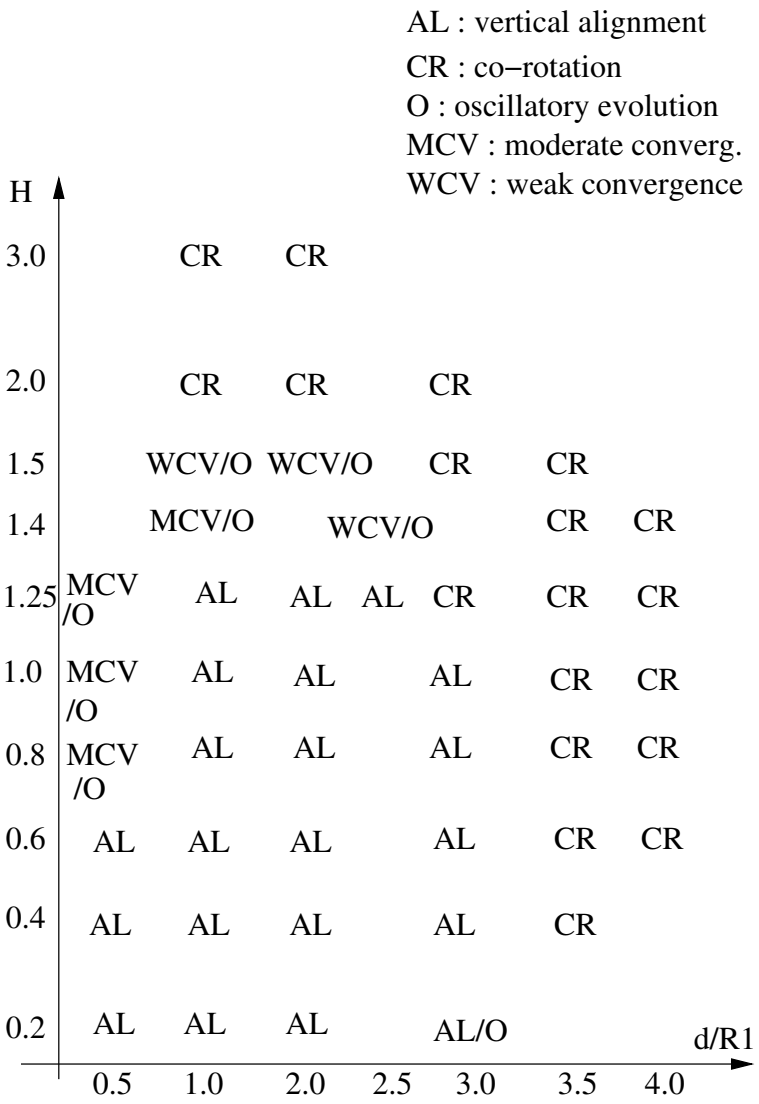

Figure 10. Nonlinear regimes of the tilted co-rotating Eady vortex, with respect to the vertical height of the domain H (or R_d/R_1) and to d/R_1 for $R_2/R_1 = 1$ and $B_2/B_1 = -1$.

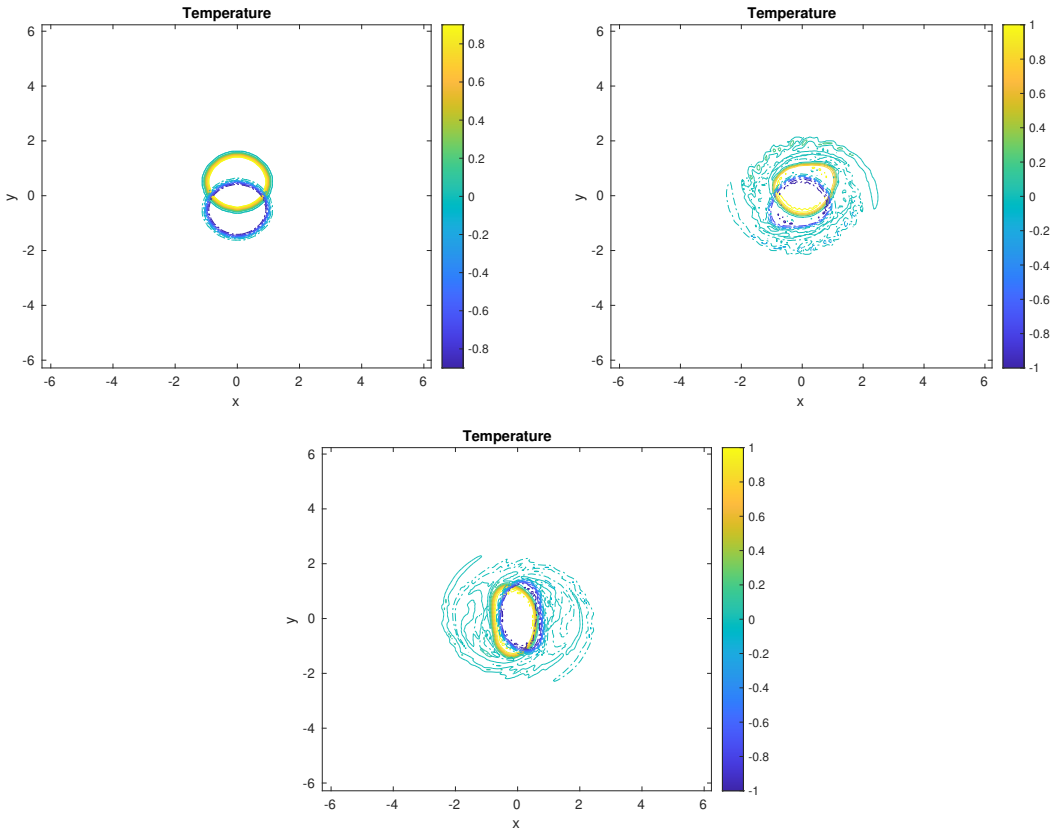

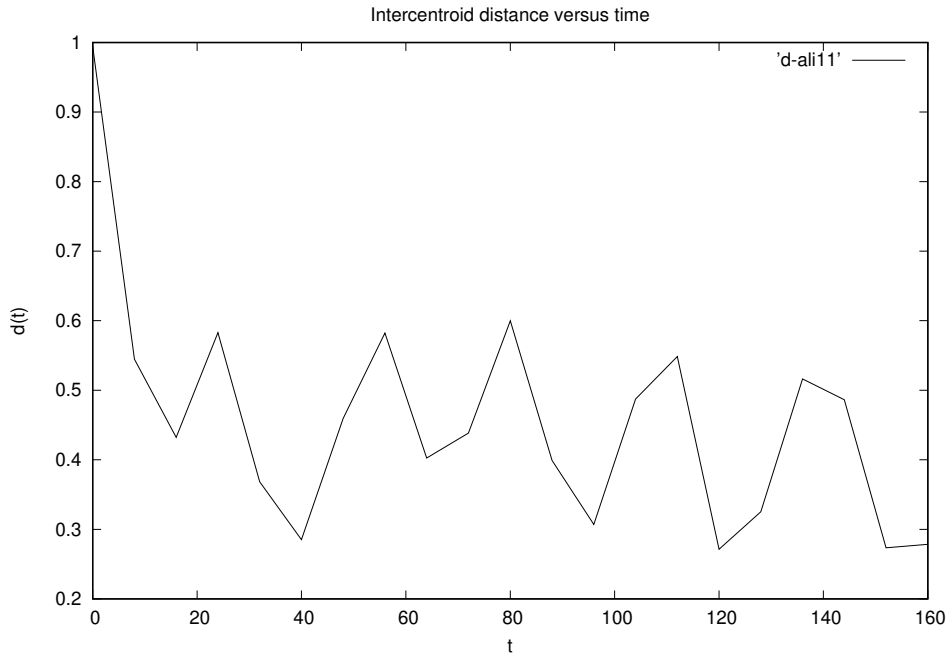

Figure 11. (Top and middle) Time series of buoyancy maps at the fluid surface (solid lines) and at the bottom (dashed lines) superimposed, showing the evolution of a tilted Eady vortex towards a vertical column. Times shown are t=0, 24, 40 model time units. The vortex parameters are $B_1 = 1, B_2 = -1$, $R_1 = R_2 = 1$, $H = R_d = 1$, $d = 1$; (bottom) Time series of the inter-centroid distance for this simulation (Colour online).

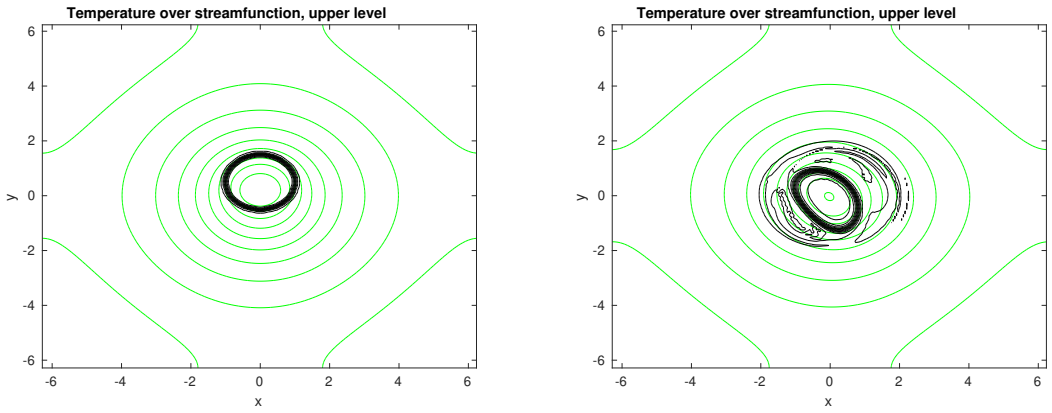

Figure 12. Maps of buoyancy (black dashed lines) superimposed on streamlines (green solid lines) for the fluid surface. Times shown are t=0, 40 model time units. The vortex parameters are $B_1 = 1, B_2 = -1$, $R_1 = R_2 = 1$, $H = R_d = 1$, $d = 1$ (Colour online).

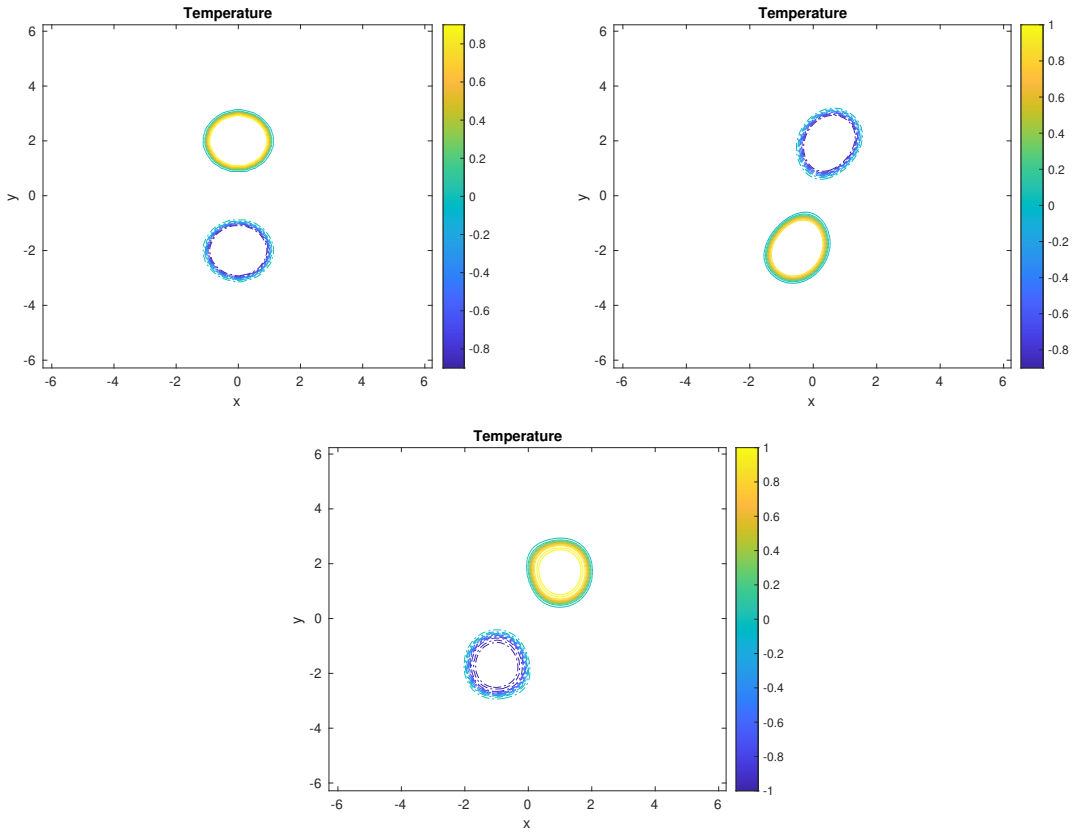

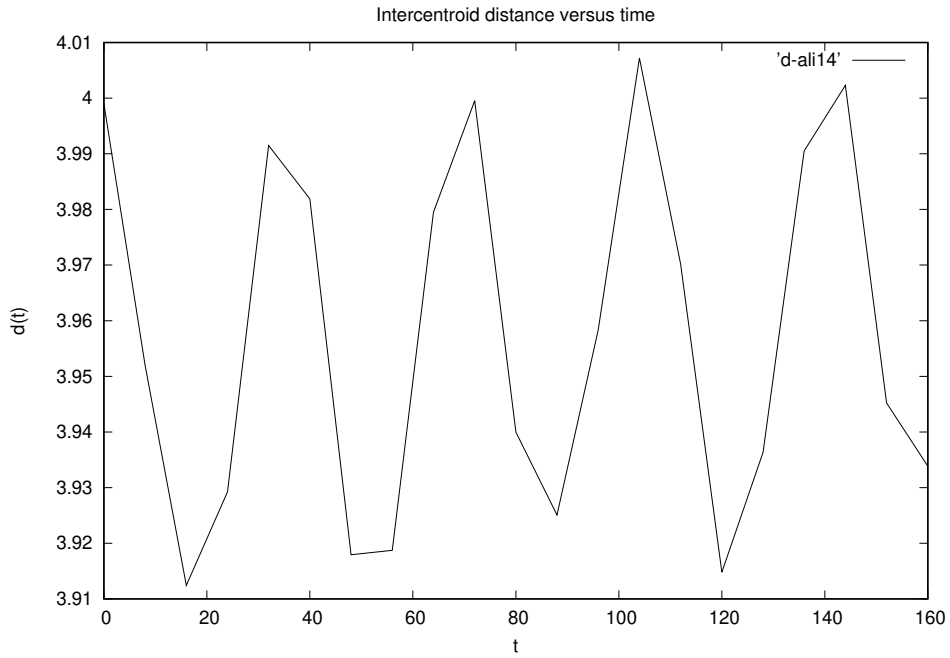

Figure 13. (Top and middle) Time series of buoyancy maps at the fluid surface (solid lines) and at the bottom (dashed lines) superimposed, showing the co-rotation of a tilted vortex around the plane center. Times shown are t=0, 64, 128 model time units. The vortex parameters are $B_1 = 1, B_2 = -1$, $R_1 = R_2 = 1$, $H = R_d = 1$, $d = 4$; (bottom) Time series of the inter-centroid distance for this simulation (Colour online).

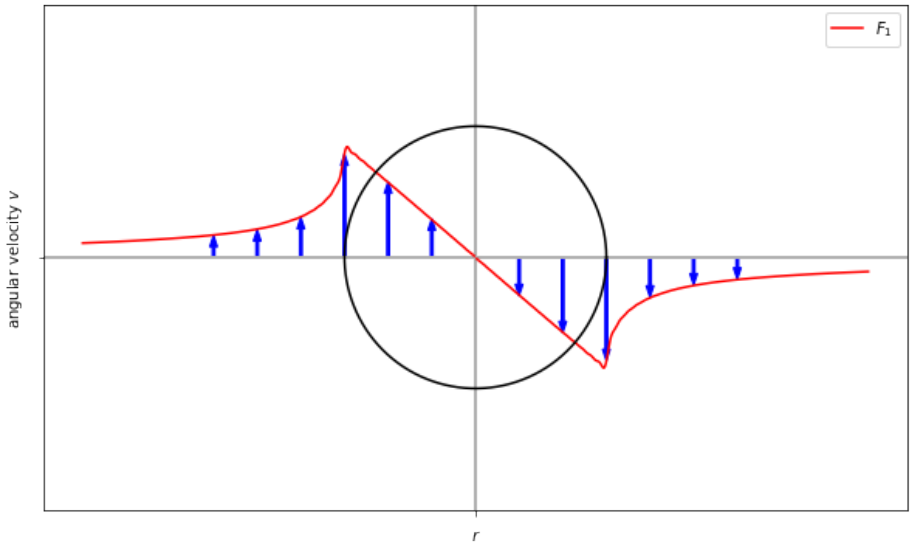

Figure A1. Graph of the angular velocity for a single hemispheric profile vortex in a 2-layer SQG model (Colour online).

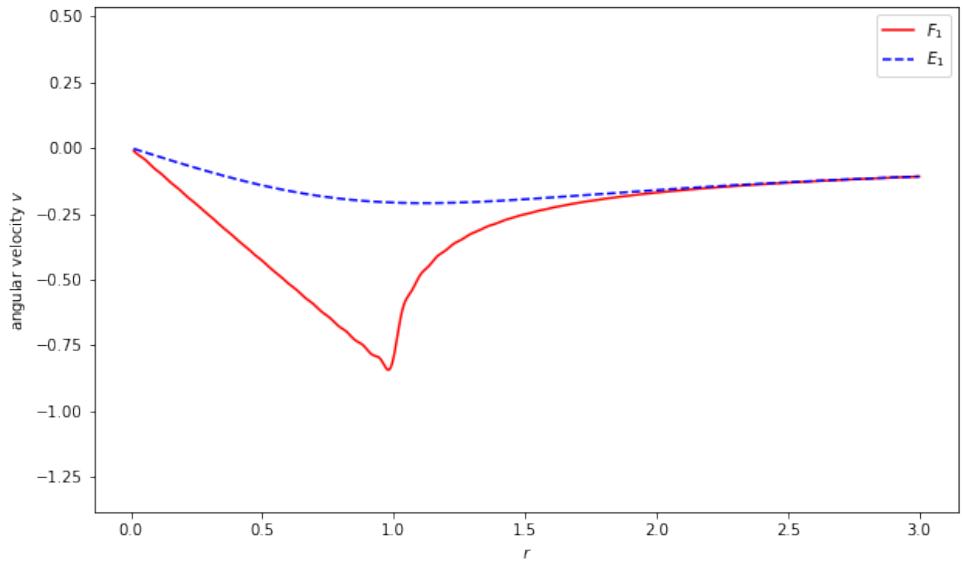

Figure A2. Graphs of the functions E_1 and F_1 for fixed $\sigma = 1$. Note that $|E_1| < |F_1|$: at the surface, the surface buoyancy influences the velocity more than the bottom buoyancy (Colour online).